



1

2

3 **Improved retrieval of land ice topography from CryoSat-2 data and its**
4 **impact for volume change estimation of the Greenland Ice Sheet**

5 Johan Nilsson¹, Alex Gardner¹, Louise Sandberg Sørensen² and Rene Forsberg²

6 ¹Jet Propulsion Laboratory, California University of Technology

7 ²DTU Space, National Space Institute, Technical University of Denmark

8 **Abstract**

9 A new methodology for retrieval of glacier and ice sheet elevations and elevation changes from
10 CryoSat-2 data is presented. Surface elevations and elevation changes determined using this
11 approach show significant improvements over ESA's publically available Cryosat-2 elevation
12 product (L2 Baseline-B). This when compared to near-coincident airborne laser altimetry from
13 NASA's Operation IceBridge and seasonal height amplitudes from the Ice, Cloud, and Elevation
14 Satellite (ICESat).

15 Applying this methodology to CryoSat-2 data collected in Interferometric Synthetic
16 Aperture mode over the high relief regions of the Greenland ice sheet we find an improvement
17 in the root-mean-square-error (RMSE) of 27% and 40% compared to ESA's L2 product in the
18 derived elevation and elevation changes, respectively. In the interior part of the ice sheet, where
19 CryoSat-2 operates in Low Resolution Mode, we find an improvement in the RMSE of 68% and
20 55% in the derived elevation and elevation changes, respectively. There is also an 86%
21 improvement in the magnitude of the seasonal amplitudes when compared to amplitudes
22 derived from ICESat data. These results indicate that the new methodology provides improved



23 tracking of the snow/ice surface with lower sensitivity to changes in near-surface dielectric
24 properties.

25 To demonstrate the utility of the new processing methodology we produce elevations,
26 elevation changes and total volume changes from Cryosat-2 data for Greenland Ice Sheet
27 during the period Jan-2011 to Jan-2015. We find that the Greenland Ice Sheet decreased in
28 volume at rate of $289 \pm 16 \text{ km}^3 \text{ a}^{-1}$, with high inter-annual variability and spatial heterogeneity in
29 rates of loss. This rate is $65 \text{ km}^3 \text{ a}^{-1}$ more negative than rates determined from ESA's L2
30 product, highlighting the importance of Cryosat-2 processing methodologies.

31 1 - Introduction

32 The European Space Agency (ESA) launched CryoSat-2 in April 2010 tasked with monitoring
33 the changes of the Earth's land and sea ice. CryoSat-2 carries a new type of Doppler/delay
34 radar altimeter (Raney, 1998) referred to as SIRAL (SAR Interferometric Radar Altimeter).
35 SIRAL operates in two different modes over land ice. Over the interior part of the ice sheets it
36 operates as a conventional pulse limited radar system, referred to as the "Low Resolution
37 Mode" (LRM). In more complex high-sloping terrain the system uses a novel second antenna to
38 operate in "Interferometric Synthetic Aperture Radar" (SIN) mode. These new features allow the
39 satellite to monitor changes in complex terrain including ice caps, glaciers and the high relief
40 marginal areas of the ice sheets. Such areas are sensitive to changes in climate and contribute
41 greatly to current rates of sea level rise, e.g., Gardner et al. (2013) and Shepherd et al. (2012).

42 Ku-band radar altimeters are insensitive to cloud cover providing superior coverage to
43 laser altimeters (e.g., ICESat) but experience significant amounts of volume scattering, the
44 characteristics of which is controlled by the time-evolving dielectric properties of the near-
45 surface snow, firn, and ice (Lacroix et al., 2008; Remy et al., 2012). These effects can have
46 large implications for the determination of mass change over a wide range of both spatial and
47 temporal scales. Changing snow conditions can introduce time-varying biases in the data that,



48 in combination with the radar signals interaction with the surface, introduce large elevation
49 biases (0.5 - 1 m) (Nilsson et al., 2015a). This, combined with other factors such as processing
50 methodology and surface topography, makes it difficult to measure small changes for much of
51 the world's ice covered regions (Arthern et al., 2001; Gray et al., 2015; Nilsson et al., 2015b).

52 The mitigation of these effects in the processing of radar altimetry data is required for
53 improved accuracy of derived temporal and spatial changes in surface elevation of glaciers and
54 ice sheets. Several studies have proposed different approaches to assess these effects and
55 improve the retrieval process of surface elevation and elevation changes from radar altimetry
56 data. These include different approaches to waveform retracking (Davis, 1993, 1997; Gray et
57 al., 2015; Helm et al., 2014) and empirical corrections to the estimated surface elevation
58 changes (Davis and Ferguson, 2004; Flament and Rémy, 2012; Sørensen et al., 2015;
59 Wingham et al., 2006b; Zwally et al., 2005, 2011). Relatively little work has been done to assess
60 methods from improving elevation and elevation changes derived from ESA's CryoSat-2 data
61 (Abulaitijiang et al., 2015; Gray et al., 2013, 2015; Helm et al., 2014).

62 Here we conduct a thorough analysis of CryoSat-2 SIN and LRM waveform retracking
63 and geolocation methodologies to design an optimal processing methodology for CryoSat-2
64 elevation retrieval over both smooth and complex ice-covered terrain. We then analyze several
65 different approaches to determining surface elevation and volume changes from the scattered
66 CryoSat-2 elevation retrievals. The overarching goal of this work is to develop robust and
67 accurate elevation retrieval algorithms that are less sensitive to changes in surface and sub-
68 surface scattering properties.

69 The new processing scheme is applied to estimate elevation and volume changes of the
70 Greenland Ice Sheet for the period January 2011 to January 2015 that are compared to change
71 estimates obtained from the ESA L2 Baseline-B surface elevation product (Bouzniac et al.,
72 2014), high accuracy airborne data from NASA IceBridge airborne topographic mapper and
73 seasonal height amplitudes estimated from Ice, Cloud, and Elevation Satellite (ICESat) data.



74 2 - Surface elevations from CryoSat-2

75 2.1 - Low Resolution Mode (LRM)

76 The LRM mode is used over the interior parts of the ice sheet, which mostly consist of low
77 sloping terrain ($0-1^\circ$). Here, SIRAL operates as a conventional pulse limited radar system with a
78 transmission frequency of 13.6 GHz (Ku-band) and has Pulse-Limited Footprint (PLF) radius of
79 approximately 1.5 km and a beam-limited footprint (BLF) radius of approximately 7.5 km over
80 flat terrain (Bouzinac, 2014). The gentle terrain allows for accurate mapping of the surface
81 elevation of the ice sheet down to decimeter-level (Brenner et al., 2007). Within the LRM
82 waveform we define the location of the surface from the leading edge of the waveform, based
83 on a fraction of the maximum amplitude of the received power. This approach is commonly
84 referred to as a threshold retracker. Following Davis et al. (1997) we use 20% threshold to
85 define the location of the surface. Davis et al. (1997) argued that a 20% threshold represents
86 the best compromise between waveforms that are entirely dominated by either volume or
87 surface scattering, making it suitable for obtaining estimates of surface elevation for most parts
88 of the Greenland Ice Sheet.

89 The CryoSat-2 LRM radar waveforms suffer from measurement noise, in the form of
90 speckle noise. Furthermore, over the steeper parts of the LRM-area the range gate tracking-
91 loop can lose track of the surface, producing non-usable waveforms. To remove bad or loss of
92 track waveforms the radar waveform (20 Hz) is first filtered using a zero-phase low pass filter to
93 reduce speckle noise on a line-by-line basis. The signal-to-noise-ratio (SNR) of the waveform is
94 then estimated and if the SNR < 0.5 dB the waveform is rejected. The SNR threshold was
95 empirically chosen to obtain a good trade-off between the quality of the measurements and
96 sampling.

97 Before the waveform can be retracked the first surface return (first major peak) is
98 identified within the range gate window. A copy of the waveform is heavily smoothed to remove



99 small-scale surface roughness signals, keeping the overall surface signal intact. The range gate
100 index of the first peak from the copy is then used to extract the leading edge of the original low
101 pass filtered waveform. Only leading edges with a peak index within the interval of 20-350 are
102 used in the retracking, as peaks before or after that indicate troublesome surface ranging. The
103 extracted leading edge is then oversampled by a factor of 100 (c.f. (Gray et al., 2013; Helm et
104 al., 2014), and the range R between the surface and satellite is determined based on the 20%
105 threshold computed according to Davis et al. (1997). The range is then corrected for several
106 atmospheric and geophysical effects relevant to land ice studies according to Bouzinac (2014).
107 The surface elevation H of the topography, relative to the WGS84 ellipsoid, is estimated as $H =$
108 $A - R$, where A is the altitude of the satellite.

109 The measured surface return over a sloping surface does not originate from the
110 satellites nadir location, but from the “Point Of Closest Approach” (POCA) to the spacecraft
111 (Brenner et al., 1983). These off-nadir returns can introduce a large range bias to the surface,
112 depending on the magnitude of surface slope, ranging from 0-120 m (Brenner et al., 1983) as
113 the measured surface height is mapped to an erroneous position (i.e. the nadir position). To
114 mitigate the effect of this error we correct the measured range and location to the POCA point
115 using an a-prior DEM, following the approach of Bamber (1994). In contrast to previous studies
116 we account also for the local surface curvature, as Remy et al. (1989) showed that accounting
117 for surface curvature in addition to surface slope significantly improve results. The surface
118 slope, aspect and curvature are estimated from an a priori DEM. The GIMP elevation model
119 (Howat et al., 2014) was used to derive surface parameters for the slope-induced error
120 correction in the LRM mode. The DEM was resampled to 2 km resolution, using bilinear
121 interpolation, prior to parameter estimation, corresponding to the pulse-limited footprint of the
122 LRM mode.

123



124 2.2 - Interferometric Synthetic Aperture Radar Mode (SIN)

125 The SIN mode is used over the marginal areas of the ice sheets and other smaller glaciated
126 areas. In these areas the SIRAL altimeter operates as a Doppler/Delay radar system (Keith
127 Raney, 1998). The Doppler/Delay radar allows for higher along-track resolution compared to
128 conventional altimetry. SIN modes allows for a 350 m resolution in along track and 1500 m
129 across track. In ordinary SAR operation only the amplitude of the radar echo is measured and
130 the phase content is discarded or ignored. With the inclusion of a second antenna on CryoSat-2,
131 interferometric SAR can also be performed. Difference in the path length between the POCA
132 and the individual antennas introduce a phase shift between the two retrieved signals that can
133 be related to the angle of arrival (look angle). The look angle can in turn be used to resolve the
134 across track (across antenna) location of the echo.

135 Multi-look processing is applied to ESA's L1B waveform product (Bouzinac, 2014) to
136 reduce the noise in the SIN waveform but it is still affected by speckle-noise, as is the case for
137 the LRM waveforms. To mitigate this effect, and to help identify the leading edge of the first
138 return, we apply speckle reduction filtering and leading edge extraction of the SIN waveforms in
139 the same way as for the LRM processing with minor changes due to differences in range gate
140 resolution. The estimated coherence C of the multi-looked waveforms is then filtered in two
141 stages; (i) all coherence measures larger than one is set to zeros (larger than one coherence
142 exists in the L1B product reason unknown). (ii) the coherence range power image is filtered
143 using a 2D 5x5 Wiener filter to remove high frequency noise. The filtering of the waveform and
144 the coherence is applied to remove noise in the recreation of the interferogram. This is further
145 discussed later.

146 The measured differential phase ϕ of the return signal is affected by phase ambiguities;
147 a sudden shift of 2π in the measured phase. To reduce phase noise and aid the phase, an
148 unwrapping of the radar interferogram I is performed according to Gray et al. (2013):



149
$$I = P \cdot C \cdot e^{-i\phi} \quad (1)$$

150 The interferogram is then filtered using a wavelet-based de-noising technique, where the real
151 and imaginary parts of the interferogram are filtered separately. The unwrapping of the
152 interferogram allows for indirect filtering of the phase, without being affected by the phase-
153 ambiguities. Phase filtering is an important consideration as it has a direct affect on accuracy of
154 the position of the ground echo. We selected a bi-orthogonal as the mother wavelet to produce
155 the wavelet coefficients decomposed into three levels. Soft thresholding was applied to detail
156 coefficients, using a heuristic threshold rule to remove noise at every level. This was done on a
157 line-by-line basis. The final filtered differential phase was then recovered by:

158
$$\phi_f = Re\{I_f\} + Im\{I_f\} \quad (2)$$

159 To resolve the phase ambiguities the filtered phase measurements require unwrapping. The
160 phase unwrapping is done on a line-by-line basis in two directions starting from the center of
161 gravity of the waveform (Wingham et al., 1986).

162 The return power distribution of a Doppler/Delay radar system shows an important
163 distinction from those from conventional pulse-limited radar systems. Here, the point
164 corresponding to the mean surface is not located at the half-power point on the leading edge,
165 but rather closer to the maximum (Wingham et al., 2006a). Therefore a new retracker has been
166 developed, closely related to the one used in Gray et al. (2013), to allow for adaptive retracking
167 of the upper parts of the leading edge of the SAR waveform. The algorithm follows the main
168 concept of the threshold retracker, developed by (Davis, 1997), but instead of a pre-defined
169 threshold it tracks the maximum gradient of the leading edge of the waveform. We refer to this
170 approach as that “Leading-edge Maximum Gradient retracker” (LMG).

171 The surface returns are geolocated using the across track look-angle θ estimated from
172 the differential phase at the retracking point according to (Wingham et al., 2006a). This, in
173 combination with the viewing geometry, is used to define the location of the surface return on



174 the ground using basic across track interferometric principles. We correct θ for the
175 interferometer surface slope error by applying the look-angle scaling factor estimated in (Galini
176 et al., 2013).

177 The along-track differential phase estimate, interpolated to the retracking point, is
178 affected by phase ambiguities not corrected for during the phase unwrapping procedure. To
179 reduce residual phase ambiguities an a priori DEM (GIMP) is used to extract the DEM surface,
180 resampled to 500 m resolution (corresponding to the along-track sampling), elevations at the
181 nadir and echolocation using bilinear interpolation. Over a sloping surface the surface return
182 should always come from a position upslope from the nadir point. Therefore the following
183 relation must hold where ($H_{echo} > H_{nadir}$) or for a more practical application ($H_{echo} - H_{nadir} > \epsilon$,
184 where ϵ is the uncertainty of the DEM used. If this relation is violated 2π is added or subtracted
185 to the individual along-track phase estimate, depending on the sign.

186 A final step is applied to correct for any lingering phase ambiguities not corrected by the
187 a priori DEM. This step uses the assumption that the along-track phase should follow a
188 consistent pattern over most part of the satellite ground track. Hence, any large discrepancies
189 from the overall pattern of the along-track phase would indicate an ambiguity. The ambiguity is
190 detected by computing the residuals of the along-track phase by removing a smoothed version.
191 If any of the residuals have a magnitude larger than π it is considered ambiguous and thus
192 corrected by adding or subtracting 2π .

193 3 - Surface elevation changes from CryoSat-2

194 3.1 – Surface fit method

195 The surface-fitting method is based on fitting a linear model to the elevations as a function of
196 time and space inside a search radius of 1 km (e.g., Howat et al., 2008; Moholdt et al., 2010;
197 Sørensen et al., 2011; Wouters et al., 2015). The linear model consists of a time-invariant



198 (static) bi-quadratic surface model to account for variable topography inside the search radius
 199 and time-variant part used to extract the temporal change in elevation. The model consists of a
 200 total of 7-parameter whereof six of the parameters (0-5) describe the bi-quadratic surface
 201 modeling function.

$$202 \quad H(x, y, t) = H_0 + a_1x + a_2y + a_3xy + a_4x^2 + a_5y^2 + a_6dt \quad (3)$$

203 The algorithm estimates the elevation change at every echolocation (or grid-node if desired) in
 204 the data set. In each solution the signal amplitude and phase are also estimated by fitting a
 205 seasonal signal model to the surface-fit elevation residuals, according to:

$$\Delta H = a_0 \cos(wt) + a_1 \sin(wt) \quad (4)$$

206 where ΔH is the elevation residuals estimated from the plan-fit model, $a_{0,1}$ are the model
 207 coefficients and t the time. The amplitude A is then defined as $A = \sqrt{a_0^2 + a_1^2}$ and the phase P
 208 as $P = \tan^{-1} \left(\frac{a_1}{a_0} \right)$.

209 To remove outliers an iterative 3σ -filter is used in the full model solution, i.e. the
 210 topography, trend and seasonal signal are removed, using a maximum of 5-iterations. For each
 211 iteration residuals (full-model) with an absolute value larger than 10 m are removed, as
 212 seasonal changes larger than 10 m are not expected (Moholdt et al., 2010; Wenlu Qi and
 213 Braun, 2013). The data inside the 1 km cap is weighted according to their distance from the
 214 estimation point according to:

$$215 \quad W = \frac{1}{\left(1 + \left[\frac{d}{\rho}\right]^2\right)} \quad (5)$$

216 where W is the estimated weight, d the distance and ρ the correlation or resolution parameter
 217 set to 500 m. The weighting allows the solution to better reflect local signal dynamics at the
 218 prediction point.

219



220 Local elevation time-series are further computed from the elevation residuals and
221 elevation trend from each solution, according to:

$$222 \quad h(t) = (t - t_0) \cdot \frac{\partial h}{\partial t} + \varepsilon(t) \quad (6)$$

223 where t is the time epochs inside the search cap, t_0 is the mean time of t , dh/dt is the elevation
224 change rate and $\varepsilon(t)$ is the elevation residual at each time epoch.

225 The elevation changes estimated from the surface-fitting method are then culled to
226 remove outliers before spatial gridding. Elevation changes with a regression error larger than 15
227 m a^{-1} are removed. The resulting surface elevations are binned at 5-km resolution for outlier
228 editing purposes. For each cell the local spatial trend is modeled as a bilinear surface, and
229 removed. The residuals are then edited using an iterative 3σ filter until the RMS converges to
230 2%.

231 3.2 – Crossover method

232 The crossover method is used to derive surface elevation at the intersection point between an
233 ascending and descending satellite ground track separated in time (Brenner et al., 2007;
234 Khvorostovsky, 2012; Zwally et al., 1989). The surface elevations and times are then estimated
235 at the crossover location for each track by linear interpolation of the two closest data points. The
236 crossover height difference is then estimated by taking the height difference between the two
237 tracks according to:

$$238 \quad dH_{12} = H_2 - H_1 + E \quad (7)$$

239 where H_1 and H_2 are the surface heights at the crossover location at time epoch t_1 and t_2 ,
240 respectively, and E is the random measurement error, including orbital, range and retracking
241 errors.

242 This approach produces crossover height differences with scattered time-epochs
243 ranging from 0-4 years. CryoSat-2 has a 369-day repeat orbit configuration with a 30-day sub-
244 cycle meaning that each crossover location will be revisited every 369 days and surrounding



245 area every 30 days. This produces annual and sub-annual crossover difference around each
246 crossover location. This fact is used to produce elevation change rates by incorporating all
247 multi-temporal crossover difference within a neighborhood of 2.5-km around each crossover
248 location. The elevation change is then estimated using the same procedure described for the
249 surface-fit method, except that a bilinear model is used to remove any spatial trends in the
250 topography of the crossover elevations according to:

$$251 \quad dH = a_0x + a_1y + a_2dt \quad (8)$$

252 where dH is the crossover height difference, dt the time difference, a_0 and a_1 the across and
253 along-track slope and a_2 the elevation change rate. This produces elevation changes
254 comparable in time and in spatial coverage with the surface-fit method. The same outlier editing
255 schemes is applied to the crossover elevation change rates as for the surface-fit method.

256 3.3 – DEM method

257 The DEM method (Helm et al., 2014; Moholdt et al., 2010; Siegfried et al., 2014) is based on
258 removing the underlying local topography from the monthly surface elevations using a DEM
259 made from the full CryoSat-2 data set (jul-2010 to feb-2015). The DEM surface elevations are
260 estimated at each echolocation using bilinear interpolation and differenced to produce elevation
261 residuals. Elevation differences with an absolute value larger than 50 m are removed from the
262 distribution. The resulting observations are culled for outliers by binning the elevation
263 differences into a 5-km resolution cells in which an iterative 3σ filter is applied. To obtain area-
264 average volume changes, the monthly observations are interpolated onto a 1 km grid using
265 Delaunay triangulation and linear interpolation. The volume change rate is estimated by fitting a
266 linear trend to the monthly volume time series, as a function of time.



267 3.4 - Gridding of sparse elevation and elevation change data

268 The gridding is done in a polar-stereographic projection with a latitude of origin at 70°N, central
269 longitude of 45°W and origin at the North Pole. The projection is referenced against the WGS-
270 84 ellipsoid and the grid-resolution. The observations derived from the surface-fit are gridded at
271 a resolution of 1x1-km, due to the high spatial sampling.

272 The method of Least Squares Collocation (LSC), described in Herzfeld (1992) is used to
273 grid the observations onto a regular grid. LSC is similar to Kriging and allows for optimal
274 interpolation and merging of data with different accuracies, using their inherent covariance
275 structure. The LSC-algorithm uses the 25 closest data points in 8-quadrants surrounding the
276 prediction point to reduce spatial biasing. The prediction equation consists of two terms where
277 the first term is the actual prediction term and the second term accounts for the non-stationary
278 part of the data, as described by:

$$y = C_{xy}(C_{xx} + N)^{-1}x + \left(1 - \sum (C_{xy}(C_{xx} + N)^{-1})\right)m(x) \quad (9)$$

279 where C_{xy} is the cross-covariance, C_{xx} is the auto-covariance, N the diagonal noise-matrix
280 consisting of the a priori RMS-error and $m(x)$ is the median value of the data inside the search
281 neighborhood.

282 The covariance of the data inside the local neighborhood is modeled as a function of
283 distance away from the prediction point using a third-order Gauss-Markov model described
284 below.

$$285 \quad C(r) = C_0 \left(1 + \frac{r}{\alpha} - \frac{r^2}{2\alpha^2}\right) e^{\left(-\frac{r}{\alpha}\right)} \quad (10)$$

286 where r is the separation distance, C_0 the local data variance and α is a scaling factor estimated
287 from the correlation length.

288

289



290 LSC interpolation provides a RMS-error for each prediction point estimated from the
291 modeled covariance of the data according to:

$$C_y = C_0 - C_{xy}(C_{xx} + N)^{-1}C_{xy}^T \quad (11)$$

292 where the RMSE of the prediction equals to $\sigma_y = (C_y)^{1/2}$ and where C_{xy}^T is the transposed cross-
293 covariance matrix.

294 The elevation changes estimated from the surface-fit and crossover methods are
295 interpolated to a regular grid using their a priori error estimated from the LSC scheme. To avoid
296 unrealistically small errors, common in the regression errors estimated over flat terrain, a
297 minimum error threshold is applied. Error values smaller than a specific threshold are set to the
298 threshold value. The threshold value is representative of the overall precision of the elevation
299 changes over flat terrain and is set to 0.2 m a^{-1} . The data are then gridded using a 50 km
300 correlation length determined from the comparison of CryoSat-2 elevation to airborne
301 measurements (Section 5).

302 The LSC algorithm is also used to generate a DEM based on the surface elevations
303 generated from the surface-fitting algorithm. The surface elevations generated from the surface-
304 fit were used as input to the gridding-algorithm. The use of surface elevations from the surface-
305 fit provides several advantages compared to the raw observations as they: provide an almost
306 equal number of observations as the raw data, have been screened for gross outliers, have
307 been low-pass filtered using the 1-km search radius, and are all reference to the same time
308 epoch. Further the RMSE error generated from the surface-fit estimated surface height can be
309 used as an a priori error for the LSC gridding procedure.

310 The DEM is generated using the same approach as for the surface elevation changes,
311 as described previously in the section. Before the gridding procedure is applied elevations $H < 0$
312 and $H > 3350 \text{ m}$ are removed from the data set. Further, elevations with a standard error larger
313 than 30 m are also removed. The elevations are binned spatially into a resolution of 1000 m and



314 inside each cell the local surface trend is removed by fitting of a planar surface, and an iterative
315 3σ filter is applied to the residuals to remove outliers.

316 4 - Surface elevations and elevation changes from ICESat

317 To assess basin-scale patterns of elevation change we compare elevation changes from
318 CryoSat-2 data to elevation changes derived from Ice, Cloud, and Elevation Satellite (ICESat)
319 data. Here we use release 33 (GLA06) data collected over the 2003-2009 period. The ICESat
320 surface heights were used to generate surface elevation changes and seasonal parameters
321 according to method M3 in Sørensen et al. (2011). The derived elevation changes were
322 corrected for the G-C offset (Borsa et al., 2014). Valid elevation retrievals were selected
323 according to Nilsson et al. (2015b). The ICESat elevation, seasonal amplitude and phase, are
324 then used for comparison with CryoSat-2 and to build continuous time series using the surface
325 fit method described in Section 3.1.

326 5 -Validation

327 Elevation and elevation change results were generated for the entire Greenland Ice Sheet using
328 CryoSat-2 data collected between Jan-2011 and Jan-2015 using the methodology presented in
329 (Sections 2-3) (JPL product) and by applying the methods of (Section 3) to ESA's CryoSat-2 L2
330 elevation products (ESA product). Surface elevations and elevation changes were validated
331 against airborne data sets obtained from NASA's Operation Ice-Bridge Airborne Topographic
332 Mapper (ATM). This mission produces both elevation and elevation changes with reported
333 vertical and temporal accuracy in the cm-level (Krabill et al., 2002).

334 The derived surface elevations from CryoSat-2 are differenced against ATM surface
335 elevations within 50 m of each ATM locations. One month of CryoSat-2 data consistent in time
336 with the ATM elevations are used for the validation to avoid biases due to temporal sampling
337 and to obtain sufficient sample size. A total of four years of campaign data are used for the



338 validation of the surface elevations (2011-2014). The residuals are edited using an iterative 3σ
339 filter to remove outliers. The accuracy and precision is estimated as the mean and standard
340 deviation of the differences, respectively. The residual distribution is further binned according to
341 surface slope estimated from the GIMP DEM (Howat et al., 2014) resampled to 500 m. The
342 sensitivity to surface slope (slope error) is then defined by fitting a 1st order polynomial to the
343 slope and height residuals. The rate estimated from the polynomial provides an indication of the
344 magnitude of the slope-induced error over the entire slope interval.

345 Surface elevation change rates estimated from three different time-periods (2012-2014,
346 2011-2013 and 2011-2014) of overlapping ATM observations (Krabill, 2014) are used to validate
347 the surface elevation changes estimated from the CryoSat-2 data. The same validation
348 methodology applied to surface elevations is applied to surface elevation changes, with a few
349 minor modifications. First the search radius is increased to 175 m to make it conform to the ATM
350 elevation change resolution of 250 m, as this search radius encloses the entire ATM grid cell.
351 Secondly the estimated mean and standard deviation are multiplied with the individual time-
352 intervals of the validation data sets to make the errors comparable.

353 For the surface-fit and crossover methods, near-coincident elevation change rates were
354 compared with ATM rates (e.g., April-2011 to April-2014). This provided three validation data
355 sets for the surface-fit method, due to its high spatial coverage. However, only the 2011-2014-
356 validation data set could be used for the crossover method, due to the lower spatial sampling of
357 the crossovers.

358 The observational error for the DEM-method is estimated similarly as for the surface-fit
359 method, with some modifications. Here, the CryoSat-2 DEM is used to de-trend the
360 corresponding months of CryoSat-2 data consistent with the months used to derive the ATM-
361 elevation changes (e.g., April 2011 to April-2014). However, the monthly spatial CryoSat-2
362 coverage does not provide adequate number of comparison points. Thus the months of March



363 and May were included in the analysis (i.e. March-May 2011 to March-May 2014) to increase
364 the number of samples.

365 The overall accuracy and precision for both the surface elevation and elevations
366 changes are then estimated by taking the weighted mean, using the number of observations as
367 weights, for each data set giving an average error for each measurement mode, as seen in
368 Table-2. The weighted average errors for each mode and method have been summarized in
369 Table-1 and Table-2 for both the ESA's and our solutions, where the values for the individual
370 campaigns can be found in the Supplementary material.

371 The estimated surface elevation changes from the three independent methods were
372 validated separately using near-coincident ATM data. In general we find the same magnitude of
373 improvement observed in the surface elevation validation analysis. The statistics of the
374 elevation change validation have been summarized in Table-2 for each method independently
375 for the two modes of instrument operation. We find the lowest RMSE errors for the surface-fit
376 method, followed by the crossover method and then the DEM method. This differs from the
377 findings of Moholdt et al. (2010) who found lower intrinsic errors for the crossover method,
378 compared to the surface-fit method when applied to ICESat data. The larger search radius used
379 for our application of the crossover method most likely explains the difference in findings
380 between studies. Further, we find that the surface-fit method provides the largest reduction in
381 RMSE for the JPL product, corresponding to 40% and 55% for the SIN and LRM-mode,
382 respectively.

383 The correlation length used to derive the number of un-correlated grid-cells, which is
384 used to estimate the standard error, was determined from a semi-variogram analysis of the
385 elevation change residuals from CryoSat-2 minus ATM using the data from the surface-fit
386 method. The comparison was done for each mode separately for all the individual campaigns
387 and multiplied with their individual time span. The semi-variogram was then computed from
388 all the time-invariant residuals, to maximize the spatial coverage, for each mode. Analysis of the



389 semi-variogram showed an approximate correlation length of 25 and 35 km for the SIN and
390 LRM-mode respectively. These correlation lengths are slightly lower than those found by
391 Sørensen et al. (2011) for their analysis of ICESat data. To be conservative we chose a
392 correlation length of 50 km for both modes.

393 Although the main goal of this study is not to derive or compare different types of DEM's
394 they do play a critical part in removing the long-wavelength topography in order to derive the
395 monthly time-series of volume change from the DEM-method. To gain insight into the overall
396 quality of our CryoSat-2 derived DEM (referred to as JPL) we compare it to three other DEM's
397 derived from other data sets. Firstly, we compare it to a DEM derived from ESA CryoSat-2 L2
398 data (referred to as ESA) gridded in the same manner as our DEM (Section 3.4). Secondly we
399 compare it to a DEM from Helm et al. (2014), also based on CryoSat-2 data from 2011-2014
400 (referred to as AWI). Thirdly, we compare to a DEM from Howat et al. (2014) (which was used
401 to derive topographical parameters and corrections for the JPL CryoSat-2 data), based on
402 photogrammetry data from 1999-2002 co-registered to ICESat elevation data from 2003-2009
403 (referred to as GIMP).

404 These data sets were then compared to IceBridge ATM elevations, spanning the four
405 different campaigns previously used for validation of the CryoSat-2 elevations. The DEM
406 elevation was estimated at each ATM location, using bilinear interpolation, and the elevation
407 difference computed as (DEM-ATM). No attempt was made to account for differences in DEM
408 and ATM epochs. The estimation of the errors of the DEM was determined in the same way as
409 for the individual CryoSat-2 surface heights. The results of the comparison have been
410 summarized in Table-3, as the weighted average of the different campaigns. The values from
411 each individual campaign can be found in the supplementary material.

412 Analyzing the overall RMSE we find that the AWI produces the lowest RMSE, followed
413 by JPL, ESA and GIMP, due to AWI's lower standard deviation. However, the best accuracy is
414 obtained by the JPL DEM, which shows the lowest elevation bias of all DEM's. The ESA derived



415 DEM shows a slightly better standard deviation than the JPL DEM, which can be explained by
416 higher data density in the marginal areas for the ESA data. The difference in density is due to
417 the SNR rejection criterion applied in our elevation processing. This smoothing can explain the
418 lower standard deviations seen for the AWI product. The GIMP data set showed higher degrees
419 of impulse noise than the other products, explaining the higher observed standard deviation.
420 This impulse noise is attributed to that local elevation change rate, which was not accounted for
421 in the creation of the DEM (Howat et al., 2014). Overall we find that the JPL DEM provides a
422 suitable compromise between resolving of local detail and the minimization of bias. Further,
423 modification to the SNR filtering criteria will likely lead to additional improvements in the DEM.

424 The impacts of the different SIN processing steps were quantified to determine the
425 importance of the different processing steps in the reduction of RMSE. A simple case study over
426 Barnes ice cap, on Baffin Island in the Canadian Arctic, was used to determine the impact of the
427 processing. Barnes was chosen as it saw a major IceBridge ATM campaign in 2011, providing
428 excellent validation coverage. The result of the case study, summarized in (Table-S1), shows
429 that the filtering of the differential phase has the highest effect on the overall RMSE followed by
430 the ambiguity correction. However, the main improvement is still located in the retracking step of
431 the processing. These steps are important to consider, as they have important implications for
432 the accuracy and precision of the measured surface elevations. This is especially true in high
433 relief areas where small changes in the look angle or phase ambiguity issues can produce large
434 elevation errors from 0-100 m in elevation (Brenner et al., 1983).

435 6 - Error analysis

436 To compute volume change errors for the three methods we divide the error budget into two
437 main components (1) the observational error (ϵ_{obs}) and (if appropriate) the interpolation error
438 (ϵ_{int}). The error budget is estimated using the root-mean-square error (RMSE) of the difference
439 between the CryoSat-2 and airborne elevation and elevation change differences as described in



440 Section 5. The overall error is then estimated using the root-sum-square (RSS) of the two error
 441 sources. The RMSE is estimated separately from the two different modes, with the total volume
 442 change error being computed as the area-weighted sum of the two components, according to:

$$443 \quad \varepsilon_{vol} = \left(\frac{A_{lrm}}{A_{tot}} \cdot \varepsilon_{lrm} + \frac{A_{sin}}{A_{tot}} \cdot \varepsilon_{sin} \right) \cdot A_{tot} \quad (12)$$

444 where A_{tot} is the total area of the ice sheet, A_{lrm} and A_{sin} are the corresponding areas covered by
 445 each mode summing to A_{tot} . The ε_{lrm} and ε_{sin} are the standard errors of the LRM and SIN
 446 computed from the airborne validation data sets.

447 The observational elevation change error is estimated from the CryoSat-2 - airborne
 448 elevation change differences (Table-2) for the three methods. The RMSE from the LRM/SIN
 449 errors are computed using Gaussian error propagation producing an observational elevation
 450 change error (ε_{obs}). For the surface-fit and the crossover method the interpolation error is
 451 estimated as the RMS of the LSC uncertainty grid. For the DEM-method only the observational
 452 error is used. The final elevation change error is then estimated by combining the two error
 453 sources using RSS according to:

$$454 \quad \varepsilon_{dh/dt} = \sqrt{\left(\frac{\sigma_{obs}}{\sqrt{N}} \right)^2 + \left(\frac{\sigma_{int}}{\sqrt{N}} \right)^2} \quad (13)$$

455 Here, N is the number of uncorrelated grid-cells estimated from empirical semi-variogram
 456 analysis of the CryoSat-2 and airborne elevation change differences, and estimated according
 457 to:

$$N = \frac{A}{\rho_c^2} \quad (14)$$

458 where A is the total area of the Greenland Ice sheet ($\sim 1.7 \times 10^6 \text{ km}^2$) and the correlation length ρ_c
 459 of 50 km.

460

461



462 7 – Results

463 The measured surface elevations from the two CryoSat-2 products (JPL vs. ESA) showed large
464 differences in both accuracy and precision of the elevation measurements, as seen in Table-1.
465 The average accuracy and precision for the LRM-mode from the two products showed values of
466 0.00 ± 0.43 m and -1.06 ± 0.89 m for the JPL and ESA products respectively. This corresponds
467 to an average reduction in RMSE of 68% for the JPL product compared to the ESA LRM L2
468 data. Further, our product shows a 33% lower residual slope error, indicating a lower sensitivity
469 to the degradation of performance as the surface slope increases.

470 Surface elevations generated from the SIN-mode showed the same type of improvement
471 as for the LRM-mode. Here, an average accuracy and precision was found to be -0.52 ± 0.58 m
472 and -0.90 ± 1.05 m for the JPL and ESA SIN elevation products respectively. This further
473 corresponds to a reduction in the average RMSE of 27% for the JPL product compared to the
474 ESA product. For the SIN-mode the JPL processing produces a slightly lower (23%) residual
475 slope error, compared to the ESA processor.

476 Larger improvements can be observed if separating the RMSE into its mean and
477 standard deviation, corresponding to the accuracy and precision of the measurements. Using
478 these definitions the analysis found that there is a 45% and 52% increase in precision for the
479 SIN and LRM mode respectively, compared to the ESA L2 product, and a 42% and 99%
480 improvement in accuracy for the respective modes.

481 The estimated surface elevation changes generated from the surface-fit method also
482 showed improvement in the estimated accuracy and precision, as seen in Table-2. Here, a
483 overall improvement in RMSE of 55% and 40% in the LRM and SIN mode, respectively, was
484 found when comparing against ESA L2 generated elevation changes from the same method.
485 The average accuracy and precision, compared to ATM generated elevation changes, was
486 found to be 0.11 ± 0.67 m (LRM) and 0.30 ± 0.58 m (SIN) for the JPL derived changes. This



487 compared to 0.25 ± 1.51 m (LRM) and 0.34 ± 1.06 m (SIN) for the ESA derived changes. This
488 corresponds to an increase in elevation change accuracy of 56% and 12% for the LRM and
489 SIN-mode, respectively, for the JPL product compared to ESA L2 elevation changes. The
490 estimated elevation changes also show an increase in precisions for the JPL product of 56%
491 and 45% for the LRM and SIN-mode, respectively, compared to its ESA counterpart.

492 The implementation of the LMG SIN retracking algorithm was found to reduce the noise
493 in the retrieved surface elevations compared to conventional threshold retracking. This is
494 exemplified over the Jakobshavn Isbræ area of the Greenland Ice Sheet (Figure S1), where
495 LMG and a leading edge threshold retracker were compared. Though roughly comparable in
496 accuracy, the LMG has a 32% improvement in precision when, compared against elevations
497 from airborne laser altimetry. The adaptive nature of the algorithm provides improved estimates
498 of surface elevation and gives good trade-off between accuracy and precision.

499 The 20% threshold retracker implemented in the LRM-mode was also found to provide
500 improved estimates of surface elevation (both in accuracy and precision) compared to the
501 model-based ESA-L2 retracker. Further, it also showed lower sensitivity to the 2012 melt event,
502 due to the lower threshold used on the leading edge of the waveform.

503 The estimated elevation changes of the Greenland Ice Sheet, excluding the peripheral
504 glaciers, over the period January 2011 to January 2015 show significant differences between
505 products (JPL and ESA) in both spatial patterns and the total magnitude (Figures 2 & 3). The
506 estimated volume change rate from the surface-fit method is -289 ± 16 km³ a⁻¹ for the JPL-
507 product and -224 ± 31 km³ a⁻¹ for the ESA-product with a mean difference of 65 km³ a⁻¹. The
508 surface-fit and crossover-method produced on the order of ~20 million and ~2.5 million usable
509 elevation changes, respectively, providing high spatial sampling. Due to the constraint put into
510 the JPL processor the ESA L2 data produced slightly more surface-fit observations (~10%), as
511 more surface elevations were accepted.



512 The ESA product produces a more positive elevation change pattern, which can be
513 attributed to the 2012 melt event that introduced a large positive bias with a magnitude of ~ 0.5
514 m (Nilsson et al., 2015). Larger differences in the marginal areas for the surface-fit methods are
515 also observed. These are particularly noticeable in eastern Greenland (near 73.5 degrees in
516 latitude Figure 2) where the ESA data shows marginal areas of rapid thinning that are not visible
517 in the JPL solution. The positive signal detected in the interior of the ESA surface-fit-solution
518 can also be found in the ESA DEM-solution, correlating well with the timing of the summer of
519 2012 melt event. These results are in agreement with earlier work demonstrating the sensitivity
520 of the ESA retracker to the changes in the volume/surface scattering ratio (Nilsson et al., 2015).

521 The three volume change methods produce consistent results from JPL derived
522 elevation changes, with a difference of less than $7 \text{ km}^3 \text{ a}^{-1}$. The spread between volume change
523 methods is larger ($50 \text{ km}^3 \text{ a}^{-1}$) when using ESA L2 data. The larger discrepancy can mostly
524 related to the sensitivity of the various methods to the melt event. The surface-fit method
525 produces the most negative number (least affected by the melt event and the lowest estimated
526 error) and is therefore taken as the most reliable estimate for both the JPL and ESA solution.

527 Comparing the estimated volume change to other studies using CryoSat-2 we find that
528 the JPL product is less negative than that estimated by Helm et al. (2014): $-375 \pm 24 \text{ km}^3 \text{ a}^{-1}$.
529 This difference can be attributed to difference in processing methodology and to the different
530 epoch of the data used by Helm et al. (2014) of January 2011 to January 2014. Using the
531 corresponding epoch the JPL data gives a volume change estimate, based on the surface-fit
532 method, of $-353 \pm 21 \text{ km}^3 \text{ a}^{-1}$, well within the stated uncertainty of Helm et al. (2014).

533 To examine the regional behavior of volume change estimates of the Greenland Ice
534 Sheet, gridded values from the three methods were divided into 8-drainage basins according to
535 Zwally et al. (2012). When analyzing the volume change time-series at the basin scale clear
536 differences can be observed in the annual and inter-annual behaviors (Figure 3). The northern
537 and interior basins (1, 2, 7, 8) all exhibit large differences (Table 4: $0 - 30 \text{ km}^3 \text{ a}^{-1}$) in the



538 estimated volume change rates due to changes in the scattering regime resulting from the 2012
539 melt event. In the majority of the southern basins (4, 5, 6, 7), located in areas with higher
540 precipitation, both products show good agreement in both trends and seasonal amplitude
541 estimated from the DEM-method.

542 The amplitude of the seasonal signal (Equation 4) estimated from the surface-fit (SF)
543 method show large differences in both magnitude and spatial variability (Figure 5). For the
544 surface-fit method a difference in amplitude of 54% is observed between the ESA and JPL
545 products, corresponding to area-averaged amplitude of 0.17 m for the JPL product and of 0.37 m
546 for ESA product. The comparison with ICESat derived amplitudes from 2003-2009 estimated in
547 (Sasgen et al., 2012) using the same methodology as used here produced an area-averaged
548 amplitude of 0.13 m, which is in good agreement with the JPL derived amplitude. This
549 agreement is also spatially consistent, as seen in (Figure 5), indicating low sensitivity to
550 seasonal changes in scattering regime of the upper snowpack. The observed difference in
551 amplitude bias, taking ICESat as the true surface amplitude while acknowledging differences in
552 epochs, is 0.03 ± 0.13 m for the JPL product and 0.21 ± 0.27 m for the ESA product. The
553 smallest differences are observed at high altitudes above 2000 m a.s.l., where the three data
554 sets show almost constant amplitude of 0.1 m (ICE/JPL) and 0.2 m (ESA), providing a factor of
555 two larger amplitude for the ESA product. Below 2000 m a.s.l., corresponding well to the
556 equilibrium-line-altitude (ELA) of the Greenland Ice Sheet, a rapid increase in amplitude is
557 observed for all products. This is especially true for the ESA product, which increases its
558 magnitude by a factor of two.

559 Analyzing the amplitude patterns on a regional drainage basin level (Figure 5c) we find
560 good agreement between JPL CryoSat-2 and ICESat amplitude with ESA data producing
561 consistently larger amplitudes. Regionally, the highest amplitudes can be observed in the SE of
562 Greenland in basins (3,4,5) and are consistent with regional precipitation patterns that show
563 high average precipitation in these areas (Bales et al., 2009; Ettema et al., 2009).



564 The seasonal phase of the peak in amplitude of the seasonal cycle is shown in (Figures
565 5b and 5c) and shows generally good agreement between the two products, providing the
566 timing of the maximum of the accumulation signal, before the onset of melt, to the months of
567 June/July for both JPL and ESA CryoSat-2 data sets. The ICESat derived seasonal phase
568 shows a higher dependence on elevation where the maximum of the accumulation signal is
569 found in late May below 2000 m and late July/August above 2000 m in elevation. The ICESat
570 discrepancies from the CryoSat-2 data are found in specific basins. Disagreements between the
571 retrieved phase of the peak amplitude from Cryosat-2 and ICESat data are due to differences in
572 temporal sampling as discussed in more detail in Section 8.1.

573 We used ICESat and CryoSat-2 derived surface heights to generate time series over
574 three regions in Northeast area of Greenland (Zachariae Isstrøm, Nioghalvfjærdsbrae (N79)
575 and Storstrømmen) for comparison purposes These areas have in recent time shown large and
576 rapid changes, which has been noted by, e.g., Khan et al. (2014). The selected areas were
577 defined using hydrological basins derived by Lewis and Smith (2009), seen in (Figure 6), and
578 were further divided into smaller areas around the termini to highlight performance for areas of
579 rapid change. The ICESat and CryoSat-2 surface heights were then used to generate annual
580 time-series from 2003-2015 using (Equation 6) in the surface fit method. The estimated 12 year
581 time series show overall comparable elevation change rates over both time periods, especially
582 in the terminus areas, providing confidence that CryoSat-2 can actually monitor changes in
583 these areas.

584 8 - Discussion

585 The CryoSat-2 processing methodology presented here is found to produce accurate and
586 precise measurements of ice sheet elevation and elevation change. The main improvements
587 have been introduced in the SIN processor with the inclusion of a new type of land ice retracker
588 (LMG), advanced phase filtering and the inclusion of a phase ambiguity correction scheme. This



589 processing approach decreased the RMSE in the surface height retrieval by approximately 27%
590 (45% and 42% improvement in precision and accuracy). This improvement further propagated
591 into the quality of the estimated elevation changes for the SIN-mode, with the same magnitude
592 of improvement (Table-2). The described SIN-processing also generated surface elevations and
593 elevation changes with lower sensitivity to the local surface slope, indicating a higher degree of
594 accuracy in the geo-location and surface range estimation.

595 The SIN processing methodology further includes a phase filtering and phase ambiguity
596 correction scheme. Visual inspections of a large number of tracks have shown more coherent
597 estimation of the surface locations in our product and further the implementation of the phase-
598 ambiguity correction greatly reduced the number of track offsets. It was also noted that a
599 relatively coarse DEM (~1 km) could be used to resolve phase ambiguities. The detection and
600 correction of phase ambiguities are relatively straightforward and rely mostly on the relative
601 accuracy of the DEM. The implementation of the phase ambiguity correction is particularly
602 important when monitoring smaller ice caps and outlet glaciers, where frequent and large track
603 offsets can bias the estimation of the underlying topography. The statistical effects of these
604 corrections have been analyzed over the Barnes Ice Cap on Ellesmere Island in the Canadian
605 Arctic and are available in Table S1.

606 The new LRM processing methodology focused on optimal retrieval of surface
607 elevations over the interior parts of the ice sheet. Here the choice of retracking threshold has
608 proven to be the critical factor to acquire high quality surface elevations and elevation changes.
609 The choice of 20% leading edge threshold level reduced the sensitivity to changes in the
610 scattering regime for low slope, high elevation areas. The functional-based retracking algorithm
611 used in the ESA LRM processor corresponds roughly to a 50% threshold level (Wingham et al.,
612 2006a), which appears to suffer from a higher sensitivity to changes in the scattering properties
613 (volume scattering) of the near-surface firn, as the range is reference higher up (later in time) on
614 the leading edge of the waveform. This effect can be seen in (Figure S1a), and that the



615 observed negative elevation bias (Table-1) for ESA-LRM (-1.0 m) fit well with the bias for the
616 50% LRM threshold value shown in Figure S1a. This makes the algorithm more sensitive to
617 annual and sub-annual changes in snow-packs volume/surface scattering ratio, which can
618 produce spurious changes in elevation due to changes in the near surface dielectric properties.
619 This is clearly shown in patterns of ESA product derived elevation changes (Figure 2b) where a
620 large elevation bias was introduced by the 2012-melt event (Nilsson et al., 2015a). The 20%
621 threshold is less sensitive to these types of changes (Table 1 & 2) and is in agreement with
622 previous work that has demonstrated that the 20% threshold best represents the mean surface
623 inside the footprint when exposed to a combination of surface and volume scattering (Davis,
624 1997).

625 Surface elevation changes, derived from multi-temporal radar altimetry observations, are
626 typically corrected for their correlation to changes in the radar waveform shape. This is to
627 reduce the effect of changes in the volume/surface scattering ratio of the ice sheets surface
628 (Davis, 2005; Flament and Rémy, 2012; Wingham et al., 2006b; Zwally et al., 2005). This
629 inherently adds to the complexity of the processing and analysis, introducing new biases and
630 error sources in the estimated parameters. For the processing approach presented here many
631 of these steps can be omitted or reduced, as they are an inherent part of the improved
632 waveform retracking. There have been attempts to remove spurious step-changes in elevation
633 resulting from sudden changes in surface scattering characteristics (caused by the 2012 melt
634 event) apparent in the ESA Baseline-B L2 data through post-processing strategies (Nilsson et
635 al., 2015c), but such approaches spread the bias over a longer period of time making the
636 “jumps” less noticeable in the time series by removing the step-change but introduces longer-
637 timescale bias of equal magnitude as the scattering layer is buried by less reflective snow and
638 low-density firn.

639 The result of the validation procedure shows a larger slope dependent bias in the ESA
640 data, both in the elevation and elevation changes (Figure 1 and Table 1 & 2). This is especially



641 true for the surface elevations, which can be seen in the figures of precision and accuracy
642 (Figure 1a and 1c), where both figures show clear linear slope for the ESA surface heights. In
643 comparison, estimated elevations from JPL-product show relatively stable statistics over the
644 entire slope range above 0.2° . The validation of the estimated surface elevation changes, seen
645 in (Figure 1b) and (Figure 1d), shows the effect of the 2012 melt event on the ESA derived
646 elevation changes below 0.2° . Further, the accuracy of the ESA derived changes show a clear
647 negative trend as function of increased surface slope. The derived precision of the surface
648 elevation change increases dramatically above 0.5° , as more complex topography is measured.

649 The JPL CryoSat-2 processing methodology produces seasonal amplitudes that are in
650 good agreement with those derived from ICESat data, further indicating the processors abilities
651 to track real and physical changes of the ice sheets surface. The current ESA implementation
652 produces noisier estimates of elevation change, as indicated by the larger standard deviations
653 of the residuals in the ESA solutions for the surface-fit and crossover-method. Figure 5 further
654 shows an amplitude bias in the ESA data compared to the corresponding ICESat reference
655 amplitudes. The bias is constant above the Greenland ELA located around 2000 m in altitude
656 but increases linearly as elevations decrease below this. The linear increase in amplitude
657 seems to be connected to the higher and more variable precipitation in the ablation zone where
658 changes in the variable snow cover produces changes in apparent surface height. This is less
659 prominent for the JPL SIN and LRM retracers. The estimated seasonal phase in Figure 5c and
660 5d show that both JPL and ESA CryoSat-2 elevation products can adequately resolve the
661 seasonal maximum of the accumulation signal. Both products provide a timing of the maximum
662 to the month of July over the entire ice sheet, independent of elevation. Assessing the CryoSat-
663 2 derived maximum one does however notice a difference between CryoSat-2 and the
664 reference ICESat dataset. This constitutes roughly a ± 1 month difference depending on the
665 elevation and the location. The cause of this difference can be attributed to the temporal
666 sampling of the ICESat mission. During the mission, due to degraded laser lifespan, data was



667 only collected in campaign mode during the spring and winter times corresponding to roughly
668 two months of measurements for each period. When the CryoSat-2 data was resampled to
669 coincide with the ICESat temporal sampling the same elevation and spatial pattern in the phase
670 of the maximum seasonal amplitude was observed as determined from the ICESat data. No
671 corresponding change in amplitude was observed. To mimic the temporal sampling of ICESat
672 the each year of the CryoSat-2 data was resampled using the total number of unique months in
673 the ICESat campaign record. This as the specific months used in the ICESat sampling changes
674 with different campaigns.

675 The three independent methods used to estimate the volume change of the Greenland
676 Ice Sheet produce consistent volume change estimates. This was especially true for volume
677 changes derived from the JPL elevations, with a discrepancy of less than $7 \text{ km}^3 \text{ a}^{-1}$ between
678 methods. All three methods provided the same estimate of integrated volume change but the
679 use of the surface-fit is recommended as it produces higher spatial sampling compared to i.e.
680 the crossover-method and lower errors. The good agreement between the methods further
681 indicates a strong reliability in the estimated volume change rates of the Greenland Ice Sheet
682 over the four-year period. It also shows the ability of CryoSat-2 to capture both small and large-
683 scale spatial patterns in the rugged topography along the coastline and in the interior of
684 Greenland. This is especially true in the major outlet glacier systems (e.g., Zachariae Isstrøm,
685 Nioghalvfjærdsbrae (N79) and Storstrømmen).

686 Studying the northern parts of the Greenland Ice Sheet we find that CryoSat-2 captures
687 both intricate and complex behavior in the marginal areas of the ice sheet. This is exemplified in
688 the NE regions of Greenland (Figure 6) near Zachariae Isstrøm, Nioghalvfjærdsbrae and
689 Storstrømmen, which all show complex and localized patterns of elevation change. Here,
690 Nioghalvfjærdsbrae shows very small changes in elevation during the observational time-span,
691 while Zachariae Isstrøm, its major neighbor shows large negative trends in elevation change.
692 The observed behavior agrees with the observations made by in recent studies by Khan et al.



693 (2014) and Mouginot et al. (2015) who document rapid retreat and drawdown of the ice-front
694 position of the two systems beginning in 2012. Storstrømmen outlet glacier system also appears
695 to show signs of rapid thinning at low elevations near the ice-front position while a large positive
696 signal is observed roughly 100 km upstream of the terminus. Rates of elevation change from
697 ICESat and CryoSat-2 data show good agreement in basin-scale trends (Figure 6b,c).

698 The observed volume change rates estimated from this study are within the range of
699 previous studies, ranging from -186 to $-309 \text{ km}^3 \text{ a}^{-1}$ for the time period 2003-2009, summarized
700 by Csatho et al. (2014). A more recent study by Helm et al. (2014: $-375 \pm 24 \text{ km}^3 \text{ a}^{-1}$) agrees
701 within uncertainties when differences in observation periods (2011 – 2014 vs. 2011 - 2015) are
702 taken into account. Assuming no changes in firn air content over respective study periods and
703 an ice density of 917 kg m^{-3} we compare estimated changes with corresponding estimates of
704 mass change our estimated rate of Greenland glacier volume change. An assessment of
705 changes in firn air content is out of the scope of this paper. Velicogna et al. (2014) estimated
706 mass loss using the Gravity Recovery and Climate Experiment satellites (GRACE) over the
707 time-period 2003-2013 provided (converted from mass) a rate of $-305 \pm 63 \text{ km}^3 \text{ a}^{-1}$ for the
708 Greenland which is inclusive of changes in Ice Sheet and peripheral glacier ice mass (-41 ± 8
709 $\text{km}^3 \text{ a}^{-1}$, Gardner et al., 2013). The estimated volume change of $-265 \text{ km}^3 \text{ a}^{-1}$ from Csatho et al.
710 (2014) and the estimated rate of $-305 \text{ km}^3 \text{ a}^{-1}$ from Velicogna et al. (2014) spans our estimated
711 rate of $-289 \text{ km}^3 \text{ a}^{-1}$.

712 9 – Summary and Conclusion

713 We conclude that the use of an adaptive retracker for the SIN-mode, based on the maximum
714 gradient method, and the use of 20% threshold retracker for the LRM-mode provide improved
715 performance to the retracker currently used for the ESA L2 elevation products. It is further
716 important, especially for the SIN-mode, to apply a leading edge discriminator to identify and
717 track the leading edge of the waveform. The functional model currently employed in the ESA



718 processor has, to the author's knowledge, no such discriminator currently implemented. This is
719 important in the SIN-mode, as it often contains multiple surface returns. The single-return model
720 applied in the ESA processor will here have issues fitting a waveform containing multiple
721 surface returns resulting in retrack jitter (Helm et al., 2014).

722 Using the new CryoSat-2 processing methodology for the LRM and SIN-mode we
723 determine the volume change of the Greenland Ice Sheet to be $-289 \pm 16 \text{ km}^3 \text{ a}^{-1}$ during the
724 period January 2011 to January 2015. The validation against airborne ATM surface elevations
725 and elevation changes showed an average improvement in the RMSE of the measured
726 elevations of 68% and 27% for the LRM and SIN mode respectively compared to ESA Baseline-
727 B L2 products. The new methodology also provide improved elevation changes with an
728 reduction in RMSE of 55% and 40% for the LRM and SIN mode respectively, compared to their
729 ESA L2 derived counterparts.

730 The methodology also showed less sensitivity to changes in near-surface scattering
731 properties than equivalent ESA products. The new processing methodology showed little effect
732 of slope-induced errors, providing better performance in the marginal areas of the ice sheets.
733 These improvements to the CryoSat-2 processing mitigate the need for post-processing to
734 correct correlations between changes in surface elevation and changes in the waveform shape
735 (i.e. backscatter and leading edge width etc.) that can introduce biases and add to the
736 complexity of the processing and analysis.

737 The presented CryoSat-2 processing methodology provides a lower intrinsic error in the
738 measured elevation, elevation change and volume change estimates, all of which will facilitate
739 improved understanding of the geophysical process leading to changes in land ice elevation.
740 Given the pending release of the ESA Baseline-C, which provides improved corrections and
741 processing mainly for the L1B product, further improvements are expected in the near future.
742 The complete set of grids used in this study are available for the public from the main author
743 (J.Nilsson) upon request and are provided in geotiff format.



744 Acknowledgement

745 We are deeply thankful for the guidance of Laurence Gray and support of David Burgess. We
746 also thank Sebastian Bjerregaard Simonsen for his plotting software and fruitful discussions.
747 This work was supported by funding from the NASA Cryosphere program. The research was
748 conducted at the Jet Propulsion Laboratory, California Institute of Technology under contract
749 with NASA.

750

751

752 References

- 753 Abulaitijiang, A., Andersen, O. B. and Stenseng, L.: Coastal sea level from inland CryoSat-2
754 interferometric SAR altimetry, *Geophys. Res. Lett.*, 42(6), 1841–1847,
755 doi:10.1002/2015GL063131, 2015.
- 756 Arthern, R., Wingham, D. and Ridout, A.: Controls on ERS altimeter measurements over ice
757 sheets: Footprint-scale topography, backscatter fluctuations, and the dependence of microwave
758 penetration depth on satellite orientation, *J. Geophys. Res. Atmos.*, 106(D24), 33471–33484,
759 doi:10.1029/2001JD000498, 2001.
- 760 Bales, R. C., Guo, Q., Shen, D., McConnell, J. R., Du, G., Burkhart, J. F., Spikes, V. B., Hanna,
761 E. and Cappelen, J.: Annual accumulation for Greenland updated using ice core data developed
762 during 2000-2006 and analysis of daily coastal meteorological data, *J. Geophys. Res. Atmos.*,
763 114(6), doi:10.1029/2008JD011208, 2009.
- 764 Bamber, J. L.: Ice sheet altimeter processing scheme, *Int. J. Remote Sens.*, 15(4), 925–938,
765 doi:10.1080/01431169408954125, 1994.
- 766 Borsa, A. A., Moholdt, G., Fricker, H. A. and Brunt, K. M.: A range correction for ICESat and its
767 potential impact on ice-sheet mass balance studies, *Cryosphere*, 8(2), 345–357, doi:10.5194/tc-



- 768 8-345-2014, 2014.
- 769 Bouzinac, C.: CryoSat product handbook, European Space Agency, ESA, 2014.
- 770 Brenner, A. C., Blindschadler, R. A., Thomas, R. H. and Zwally, H. J.: Slope-induced errors in
771 radar altimetry over continental ice sheets, *J. Geophys. Res.*, 88(C3), 1617,
772 doi:10.1029/JC088iC03p01617, 1983.
- 773 Brenner, A. C. ., DiMarzio, J. P. . and Zwally, H. J. .: Precision and accuracy of satellite radar
774 and laser altimeter data over the continental ice sheets, *IEEE Trans. Geosci. Remote Sens.*,
775 45(2), 321–331, doi:10.1109/TGRS.2006.887172, 2007.
- 776 Csatho, B. M., Schenk, A. F., van der Veen, C. J., Babonis, G., Duncan, K., Rezvanbehbahani,
777 S., van den Broeke, M. R., Simonsen, S. B., Nagarajan, S. and van Angelen, J. H.: Laser
778 altimetry reveals complex pattern of Greenland Ice Sheet dynamics., *Proc. Natl. Acad. Sci. U. S.*
779 *A.*, 111(52), 18478–83, doi:10.1073/pnas.1411680112, 2014.
- 780 Davis, C. H.: Surface and volume scattering retracking algorithm for ice sheet satellite altimetry,
781 *IEEE Trans. Geosci. Remote Sens.*, 31(4), 811–818, doi:10.1109/36.239903, 1993.
- 782 Davis, C. H.: A robust threshold retracking algorithm for measuring ice-sheet surface elevation
783 change from satellite radar altimeters, *IEEE Trans. Geosci. Remote Sens.*, 35(4), 974–979,
784 doi:10.1109/36.602540, 1997.
- 785 Davis, C. H.: Snowfall-Driven Growth in East Antarctic Ice Sheet Mitigates Recent Sea-Level
786 Rise, *Science (80-.)*, 308(5730), 1898–1901, doi:10.1126/science.1110662, 2005.
- 787 Davis, C. H. and Ferguson, A. C.: Elevation change of the antarctic ice sheet, 1995-2000, from
788 ERS-2 satellite radar altimetry, *IEEE Trans. Geosci. Remote Sens.*, 42(11), 2437–2445,
789 doi:10.1109/TGRS.2004.836789, 2004.
- 790 Ettema, J., Van Den Broeke, M. R., Van Meijgaard, E., Van De Berg, W. J., Bamber, J. L., Box,
791 J. E. and Bales, R. C.: Higher surface mass balance of the Greenland ice sheet revealed by
792 high-resolution climate modeling, *Geophys. Res. Lett.*, 36(12), 1–5,
793 doi:10.1029/2009GL038110, 2009.



- 794 Flament, T. and Rémy, F.: Dynamic thinning of Antarctic glaciers from along-track repeat radar
795 altimetry, *J. Glaciol.*, 58(211), 830–840, doi:10.3189/2012JoG11J118, 2012.
- 796 Galin, N., Wingham, D. J., Cullen, R., Fornari, M., Smith, W. H. F. and Abdalla, S.: Calibration of
797 the CryoSat-2 interferometer and measurement of across-track ocean slope, *IEEE Trans.*
798 *Geosci. Remote Sens.*, 51(1), 57–72, doi:10.1109/TGRS.2012.2200298, 2013.
- 799 Gardner, A. S., Moholdt, G., Cogley, J. G., Wouters, B., Arendt, A. a, Wahr, J., Berthier, E.,
800 Hock, R., Pfeffer, W. T., Kaser, G., Ligtenberg, S. R. M., Bolch, T., Sharp, M. J., Hagen, J. O.,
801 van den Broeke, M. R. and Paul, F.: A reconciled estimate of glacier contributions to sea level
802 rise: 2003 to 2009., *Science*, 340(6134), 852–7, doi:10.1126/science.1234532, 2013.
- 803 Gray, L., Burgess, D., Copland, L., Cullen, R., Galin, N., Hawley, R. and Helm, V.:
804 Interferometric swath processing of Cryosat data for glacial ice topography, *Cryosph.*, 7(6),
805 1857–1867, doi:10.5194/tc-7-1857-2013, 2013.
- 806 Gray, L., Burgess, D., Copland, L., Demuth, M. N., Dunse, T., Langley, K. and Schuler, T. V.:
807 CryoSat-2 delivers monthly and inter-annual surface elevation change for Arctic ice caps,
808 *Cryosph.*, 9(5), 1895–1913, doi:10.5194/tc-9-1895-2015, 2015.
- 809 Helm, V., Humbert, A. and Miller, H.: Elevation and elevation change of Greenland and
810 Antarctica derived from CryoSat-2, *Cryosph.*, 8(4), 1539–1559, doi:10.5194/tc-8-1539-2014,
811 2014.
- 812 Herzfeld, U. C.: Least-squares collocation, geophysical inverse theory and geostatistics: a bird's
813 eye view, *Geophys. J. Int.*, 111(2), 237–249, doi:10.1111/j.1365-246X.1992.tb00573.x, 1992.
- 814 Howat, I. M., Smith, B. E., Joughin, I. and Scambos, T. A.: Rates of southeast Greenland ice
815 volume loss from combined ICESat and ASTER observations, *Geophys. Res. Lett.*, 35(17), 1–5,
816 doi:10.1029/2008GL034496, 2008.
- 817 Howat, I. M., Negrete, A. and Smith, B. E.: The Greenland Ice Mapping Project (GIMP) land
818 classification and surface elevation data sets, *Cryosph.*, 8(4), 1509–1518, doi:10.5194/tc-8-
819 1509-2014, 2014.



- 820 Keith Raney, R.: The delay/doppler radar altimeter, *IEEE Trans. Geosci. Remote Sens.*, 36(5),
821 1578–1588, doi:10.1109/36.718861, 1998.
- 822 Khan, S. a, Kjaer, K. H., Bevis, M., Bamber, J. L., Wahr, J., Kjeldsen, K. K., Bjork, A. a,
823 Korsgaard, N. J., Stearns, L. a, van den Broeke, M. R., Liu, L., Larsen, N. K. and Muresan, I. S.:
824 Sustained mass loss of the northeast Greenland ice sheet triggered by regional warming, *Nat.*
825 *Clim. Chang.*, 4(4), 292–299, doi:10.1038/nclimate2161, 2014.
- 826 Khvorostovsky, K. S.: Merging and analysis of elevation time series over Greenland Ice Sheet
827 From Satellite Radar Altimetry, *IEEE Trans. Geosci. Remote Sens.*, 50(1), 23–36,
828 doi:10.1109/TGRS.2011.2160071, 2012.
- 829 Krabill, W. B., Abdalati, W., Frederick, E. B., Manizade, S. S., Martin, C. F., Sonntag, J. G.,
830 Swift, R. N., Thomas, R. H. and Yungel, J. G.: Airborne laser altimetry mapping of the
831 Greenland ice sheet : application to mass balance assessment, *J. Geodyn.*, 34, 357–376,
832 doi:10.1016/s0264-3707(02)00048-0, 2002.
- 833 Krabill, W. B.: *IceBridge ATM L4 Surface Elevation Rate of Change* [IDHDT4.001], Boulder,
834 Colorado USA, NASA DAAC at the National Snow and Ice Data Center,
835 <http://dx.doi.org/10.5067/BCW6CI3TXOCY>, 2014 (updated 2015).
- 836 Lacroix, P., Dechambre, M., Legrésy, B., Blarel, F. and Rémy, F.: On the use of the dual-
837 frequency ENVISAT altimeter to determine snowpack properties of the Antarctic ice sheet,
838 *Remote Sens. Environ.*, 112, 1712–1729, doi:10.1016/j.rse.2007.08.022, 2008.
- 839 Lewis, S. M. and Smith, L. C.: Hydrologic drainage of the Greenland Ice Sheet, *Hydrol.*
840 *Process.*, 23(14), 2004–2011, doi:10.1002/hyp.7343, 2009.
- 841 Moholdt, G., Nuth, C., Hagen, J. O. and Kohler, J.: Recent elevation changes of Svalbard
842 glaciers derived from ICESat laser altimetry, *Remote Sens. Environ.*, 114(11), 2756–2767,
843 doi:10.1016/j.rse.2010.06.008, 2010.
- 844 Mougintot, J., Rignot, E., Scheuchl, B., Fenty, I., Khazendar, A., Morlighem, M., Buzzi, A. and
845 Paden, J.: Fast retreat of Zachariae Isstrom, northeast Greenland, *Science* (80-.), 350(6266),



- 846 1357–1361, doi:10.1126/science.aac7111, 2015.
- 847 Nilsson, J., Vallelonga, P., Simonsen, S. B., Sørensen, L. S., Forsberg, R., Dahl-Jensen, D.,
848 Hirabayashi, M., Goto-Azuma, K., Hvidberg, C. S., Kjaer, H. A. and Satow, K.: Greenland 2012
849 melt event effects on CryoSat-2 radar altimetry, *Geophys. Res. Lett.*, 42(10), 3919–3926,
850 doi:10.1002/2015GL063296, 2015a.
- 851 Nilsson, J., Sandberg Sørensen, L., Barletta, V. R. and Forsberg, R.: Mass changes in Arctic ice
852 caps and glaciers: implications of regionalizing elevation changes, *Cryosph.*, 9(1), 139–150,
853 doi:10.5194/tc-9-139-2015, 2015b.
- 854 Nilsson, J., Forsberg, F., and Sørensen L.S.: Cryosphere monitoring from satellites and
855 aircrafts, Ph.D. thesis, Technical University of Denmark, Kgs. Lyngby, 2015c.
- 856 Remy, F., Mazzega, P., Houry, S., Brossier, C. and Minster, J. F.: Mapping of the topography of
857 continental ice by inversion of satellite-altimeter data, *J. Glaciol.*, 35(119), 98–107,
858 doi:10.3189/002214389793701419, 1989.
- 859 Remy, F., Flament, T., Blarel, F. and Benveniste, J.: Radar altimetry measurements over
860 antarctic ice sheet: A focus on antenna polarization and change in backscatter problems, *Adv.*
861 *Sp. Res.*, 50(8), 998–1006, doi:10.1016/j.asr.2012.04.003, 2012.
- 862 Sasgen, I., van den Broeke, M., Bamber, J. L., Rignot, E., Sørensen, L. S., Wouters, B.,
863 Martinec, Z., Velicogna, I. and Simonsen, S. B.: Timing and origin of recent regional ice-mass
864 loss in Greenland, *Earth Planet. Sci. Lett.*, 333-334, 293–303, doi:10.1016/j.epsl.2012.03.033,
865 2012.
- 866 Shepherd, A., Ivins, E. R., A, G., Barletta, V. R., Bentley, M. J., Bettadpur, S., Briggs, K. H.,
867 Bromwich, D. H., Forsberg, R., Galin, N., Horwath, M., Jacobs, S., Joughin, I., King, M. A.,
868 Lenaerts, J. T. M., Li, J., Ligtenberg, S. R. M., Luckman, A., Luthcke, S. B., McMillan, M.,
869 Meister, R., Milne, G., Mouginit, J., Muir, A., Nicolas, J. P., Paden, J., Payne, A. J., Pritchard,
870 H., Rignot, E., Rott, H., Sorensen, L. S., Scambos, T. A., Scheuchl, B., Schrama, E. J. O.,
871 Smith, B., Sundal, A. V., van Angelen, J. H., van de Berg, W. J., van den Broeke, M. R.,



872 Vaughan, D. G., Velicogna, I., Wahr, J., Whitehouse, P. L., Wingham, D. J., Yi, D., Young, D.
873 and Zwally, H. J.: A reconciled estimate of Ice-sheet mass balance, *Science* (80-.), 338(6111),
874 1183–1189, doi:10.1126/science.1228102, 2012.

875 Siegfried, M. R., Fricker, H. A., Roberts, M., Scambos, T. A. and Tulaczyk, S.: A decade of West
876 Antarctic subglacial lake interactions from combined ICESat and CryoSat-2 altimetry, *Geophys.*
877 *Res. Lett.*, 41(3), 891–898, doi:10.1002/2013GL058616, 2014.

878 Sørensen, L. S., Simonsen, S. B., Nielsen, K., Lucas-Picher, P., Spada, G., Adalgeirsdottir, G.,
879 Forsberg, R. and Hvidberg, C. S.: Mass balance of the Greenland ice sheet (2003-2008) from
880 ICESat data - The impact of interpolation, sampling and firn density, *Cryosphere*, 5(1), 173–186,
881 doi:10.5194/tc-5-173-2011, 2011.

882 Sørensen, L. S., Simonsen, S. B., Meister, R., Forsberg, R., Levinsen, J. F. and Flament, T.:
883 Envisat-derived elevation changes of the Greenland ice sheet, and a comparison with ICESat
884 results in the accumulation area, *Remote Sens. Environ.*, 160, 56–62,
885 doi:10.1016/j.rse.2014.12.022, 2015.

886 Velicogna, I., Sutterley, T. C. and Van Den Broeke, M. R.: Regional acceleration in ice mass
887 loss from Greenland and Antarctica using GRACE time-variable gravity data, *Geophys. Res.*
888 *Lett.*, 41(22), 8130–8137, doi:10.1002/2014GL061052, 2014.

889 Wenlu Qi and Braun, A.: Accelerated elevation change of Greenland's Jakobshavn glacier
890 observed by ICESat and IceBridge, *IEEE Geosci. Remote Sens. Lett.*, 10(5), 1133–1137,
891 doi:10.1109/LGRS.2012.2231954, 2013.

892 Wingham, D. J., Rapley, C. G. and Griffiths, H.: New techniques in satellite altimeter tracking
893 systems, in *Proceedings of the IGARSS Symposium, Zurich*, pp. 1339–1344, ESA SP-254,
894 Zurich., 1986.

895 Wingham, D. J., Francis, C. R., Baker, S., Bouzinac, C., Brockley, D., Cullen, R., de Chateau-
896 Thierry, P., Laxon, S. W., Mallow, U., Mavrocordatos, C., Phalippou, L., Ratier, G., Rey, L.,
897 Rostan, F., Viau, P. and Wallis, D. W.: CryoSat: A mission to determine the fluctuations in



898 Earth's land and marine ice fields, *Adv. Sp. Res.*, 37(4), 841–871,
899 doi:10.1016/j.asr.2005.07.027, 2006a.

900 Wingham, D. J., Shepherd, a, Muir, a and Marshall, G. J.: Mass balance of the Antarctic ice
901 sheet., *Philos. Trans. A. Math. Phys. Eng. Sci.*, 364(1844), 1627–35,
902 doi:10.1098/rsta.2006.1792, 2006b.

903 Wouters, B., Martin-Espanol, A., Helm, V., Flament, T., van Wessem, J. M., Ligtenberg, S. R.
904 M., van den Broeke, M. R. and Bamber, J. L.: Dynamic thinning of glaciers on the Southern
905 Antarctic Peninsula, *Science (80-.)*, 348(6237), 899–903, doi:10.1126/science.aaa5727, 2015.

906 Zwally, H. J., Bindschadler, R. a, Brenner, a C., Major, J. a and Marsh, J. G.: Growth of
907 greenland ice sheet: measurement., *Science*, 246(4937), 1587–1589,
908 doi:10.1126/science.246.4937.1587, 1989.

909 Zwally, H. J., Giovinetto, M. B., Li, J., Cornejo, H. G. and Beckley, M. a: Mass changes of the
910 Greenland and Antarctica ice sheets and shelves and contributions to sea level rise: 1992-2002,
911 *J. Glaciol.*, 51(175), 509, doi:10.3189/172756505781829007, 2005.

912 Zwally, H. J., Jun, L., Brenner, A. C., Beckley, M., Cornejo, H. G., Dimarzio, J., Giovinetto, M.
913 B., Neumann, T. a, Robbins, J., Saba, J. L., Donghui, Y. and Wang, W.: Greenland ice sheet
914 mass balance: distribution of increased mass loss with climate warming; 2003–07 versus 1992–
915 2002, *J. Glaciol.*, 57(201), 88–102, doi:10.3189/002214311795306682, 2011.

916 Zwally, H. Jay, Mario B. Giovinetto, Matthew A. Beckley, and Jack L. Saba: Antarctic and
917 Greenland drainage systems, GSFC Cryospheric Sciences Laboratory, at
918 http://icesat4.gsfc.nasa.gov/cryo_data/ant_grn_drainage_systems.php, 2012



919 Tables:

920 *Table 1: Accuracy (Mean), precision (SD), the total RMS-error (RMSE) and the residual slope*
921 *error (SE) of surface elevation from CryoSat-2 observations compared to IceBridge ATM*
922 *elevations. Here, the LRM mode represents the interior of the ice sheet and SIN the marginal*
923 *high relief areas.*

JPL	Mean (m)	SD (m)	RMSE (m)	SE (m/deg)
LRM	0.00	0.43	0.45	1.05
SIN	-0.52	0.58	0.82	0.52
ESA	Mean (m)	SD (m)	RMSE (m)	SE (m/deg)
LRM	-1.06	0.89	1.40	1.57
SIN	-0.90	1.05	1.13	0.68

924



925 *Table 2: Accuracy (Mean), precision (SD), the total RMS-error (RMSE) and the residual slope*
 926 *error (SE) of surface elevation changes from CryoSat-2 derived from three independent*
 927 *methods [Surface Fit (SF), Crossover (XO) and the DEM method (DM)], compared to IceBridge*
 928 *ATM data.*

JPL - LRM	Mean (m)	SD (m)	RMSE (m)	SE (m/deg)
SF	0.11	0.67	0.70	0.39
XO	0.24	0.72	0.78	1.23
DM	0.21	1.92	1.95	0.68
ESA - LRM	Mean (m)	SD (m)	RMSE (m)	SE (m/deg)
SF	0.25	1.51	1.57	1.40
XO	0.60	1.02	1.20	5.01
DM	0.27	2.40	2.56	3.37
JPL - SIN	Mean (m)	SD (m)	RMSE (m)	SE (m/deg)
SF	0.30	0.58	0.66	0.52
XO	-0.60	1.26	1.26	0.60
DM	0.26	3.59	3.72	4.97
ESA - SIN	Mean (m)	SD (m)	RMSE (m)	SE (m/deg)
SF	0.34	1.06	1.11	0.39
XO	-0.21	1.44	1.44	0.81
DM	0.31	5.01	5.03	3.07

929
930



931 Table 3: Validation of four different DEMs, compared to IceBridge ATM elevation data. Based
932 on the weighted (number of samples) average of the four different ATM campaigns from 2011 to
933 2014. Elevation values at each ATM location were estimated by bilinear interpolation for each
934 DEM product.

DEM	Mean (m)	SD (m)	RMSE (m)	SE (m/deg)
AWI	-1.35	5.95	6.12	1.35
GIMP	-1.13	7.22	7.32	0.84
JPL	-0.87	6.31	6.39	1.06
ESA	-2.83	6.13	6.76	1.62

935
936



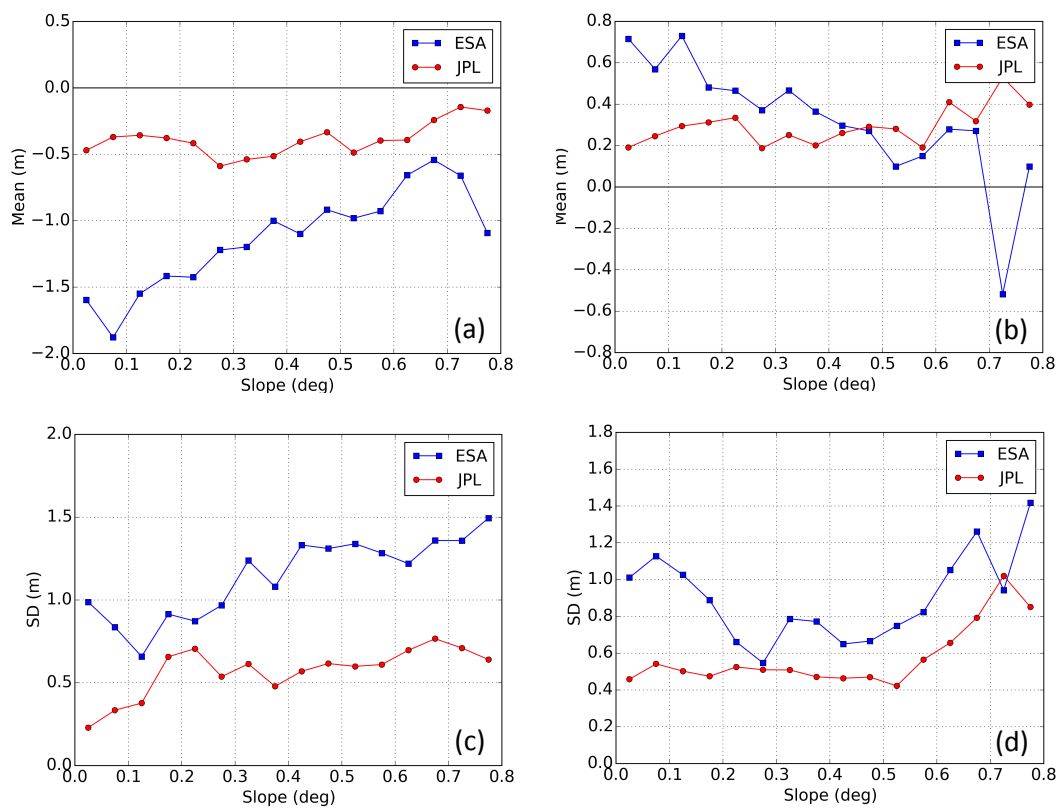
937 *Table 4: Individual basin volume changes (km^3a^{-1}) for the Surface-Fit (SF), Crossover (XO) and*
 938 *DEM (DM) method for the JPL and ESA product for the time period Jan-2011 to Jan-2015, with*
 939 *corresponding volumetric error.*

Basin	DM - JPL	SF - JPL	XO - JPL	DM - ESA	SF - ESA	XO - ESA
1	-21 ± 26	-26 ± 6	-23 ± 9	-8 ± 34	-9 ± 12	-11 ± 12
2	0 ± 26	5 ± 7	0 ± 10	25 ± 35	31 ± 14	30 ± 13
3	-48 ± 27	-38 ± 6	-34 ± 15	-26 ± 36	-46 ± 13	-31 ± 20
4	-39 ± 20	-36 ± 4	-37 ± 11	-46 ± 27	-42 ± 9	-16 ± 14
5	-20 ± 11	-19 ± 2	-27 ± 8	-13 ± 15	-19 ± 4	-6 ± 9
6	-75 ± 22	-72 ± 6	-71 ± 10	-79 ± 29	-75 ± 11	-79 ± 18
7	-46 ± 20	-56 ± 6	-51 ± 10	-36 ± 27	-41 ± 12	-35 ± 14
8	-45 ± 25	-48 ± 6	-45 ± 10	-21 ± 33	-23 ± 13	-27 ± 14
TOT	-295 ± 64	-289 ± 16	-288 ± 30	-203 ± 85	-224 ± 31	-174 ± 41

940



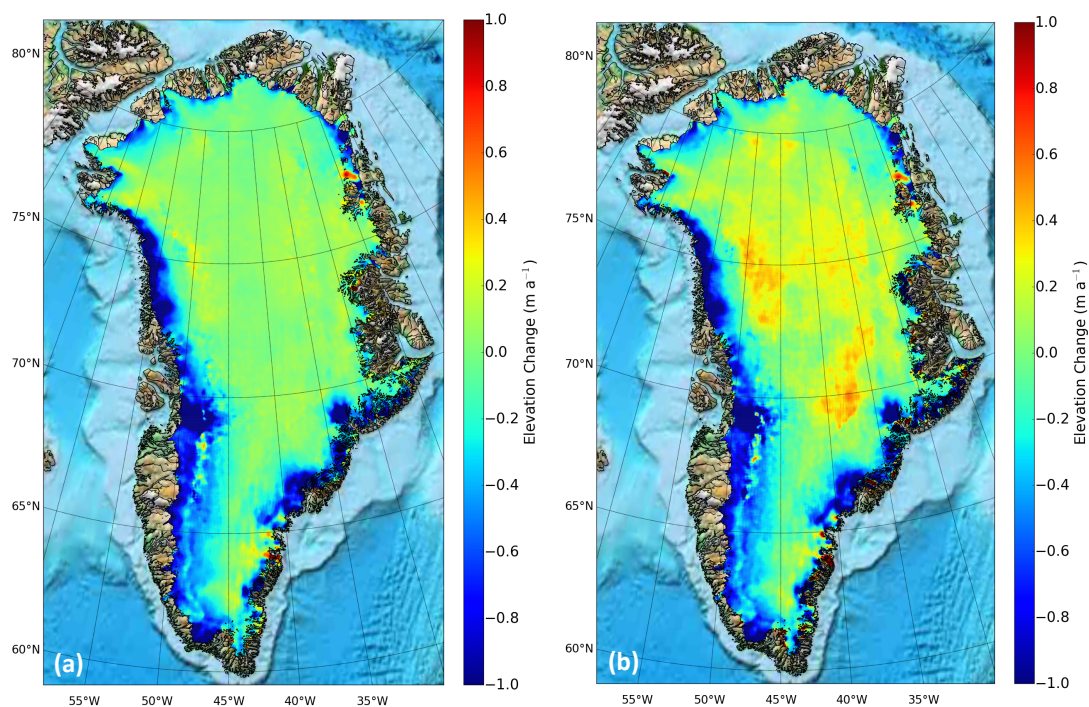
941 Figures:



942

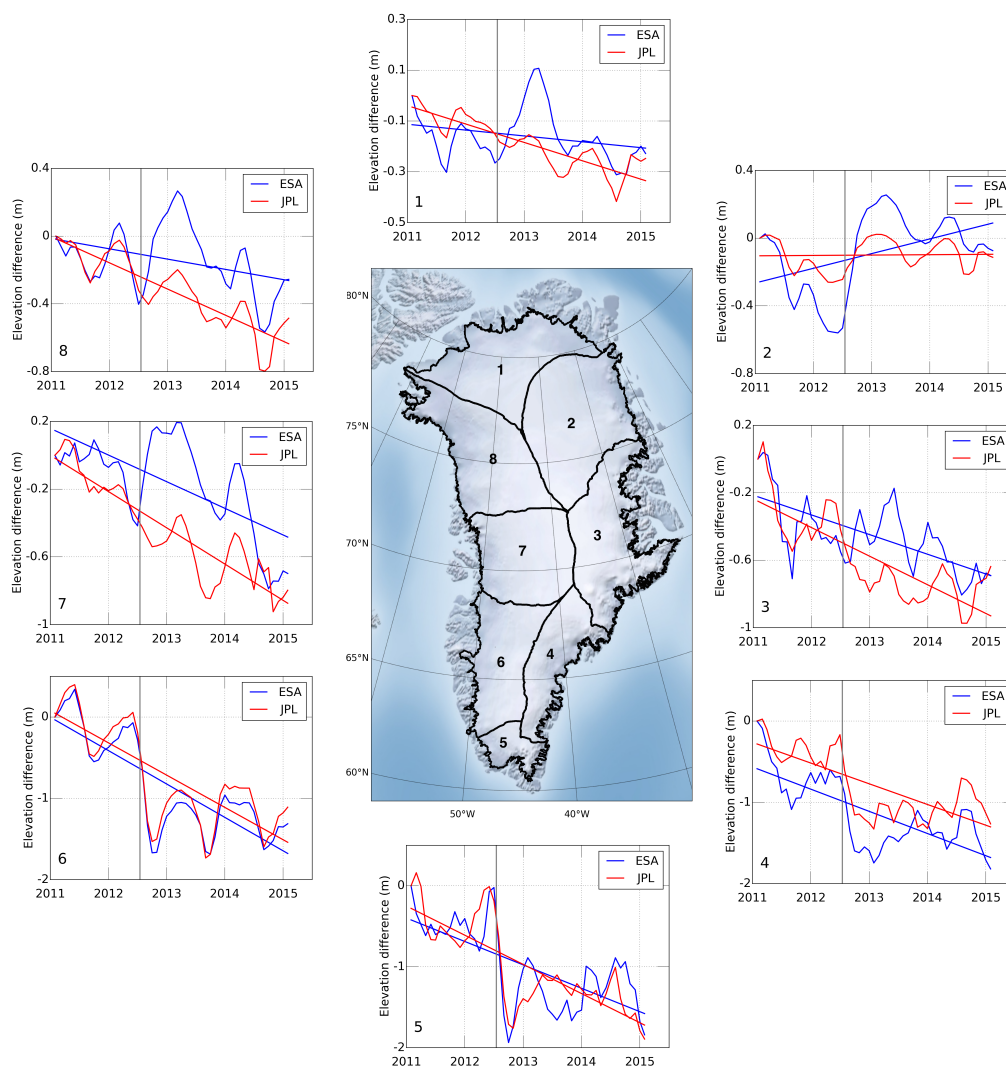
943 *Figure 1: Validation of surface elevations (2012) (a,c) and surface elevation changes (2011-*
944 *2014) (b,d) compared to IceBridge ATM, as a function of surface slope. The accuracy of the*
945 *measurement is defined as the mean-value (Mean) of the CryoSat-2-ATM residuals and the*
946 *precision as the standard deviation (SD).*

947



948

949 *Figure 2: 2011-2015 elevation changes estimated from the surface-fit methods for the JPL (a)*
950 *and ESA L2 products (b). The JPL product produced a total volume change of $-289 \pm 16 \text{ km}^3 \text{ a}^{-1}$*
951 *while the estimated total volume change of the ESA product totaled $-224 \pm 31 \text{ km}^3 \text{ a}^{-1}$. This*
952 *corresponds to -29 versus $38 \text{ km}^3 \text{ a}^{-1}$ ($H > 2000 \text{ m}$) and -259 versus $-262 \text{ km}^3 \text{ a}^{-1}$ ($H < 2000 \text{ m}$)*
953 *for the JPL and ESA product respectively. Images have been smoothed with a 5 km median*
954 *filter for visualization purposes.*

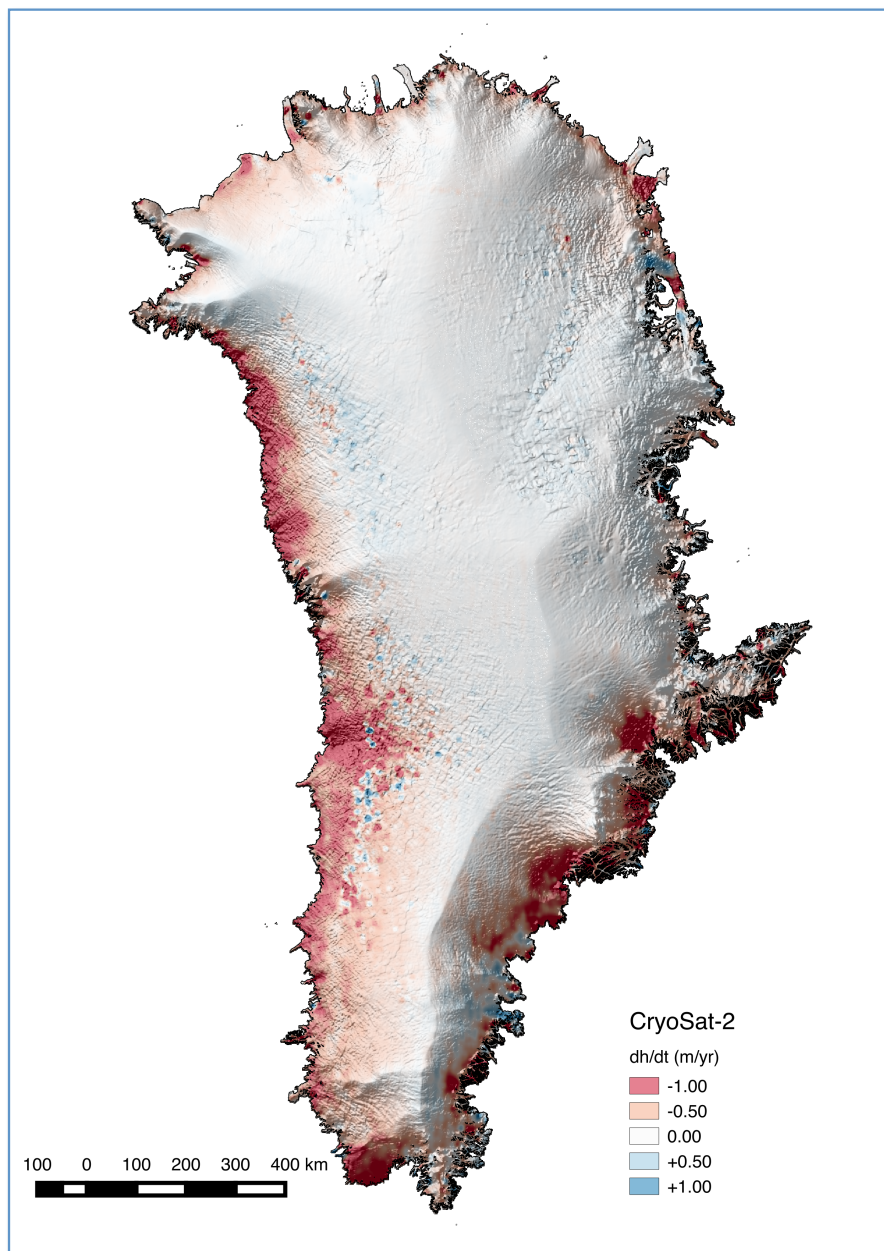


955

956 *Figure 3. Monthly elevation change time-series for 8 large drainage basins of the Greenland Ice*

957 *Sheet. Time-series have been smoothed using a 3-month moving average for improved*

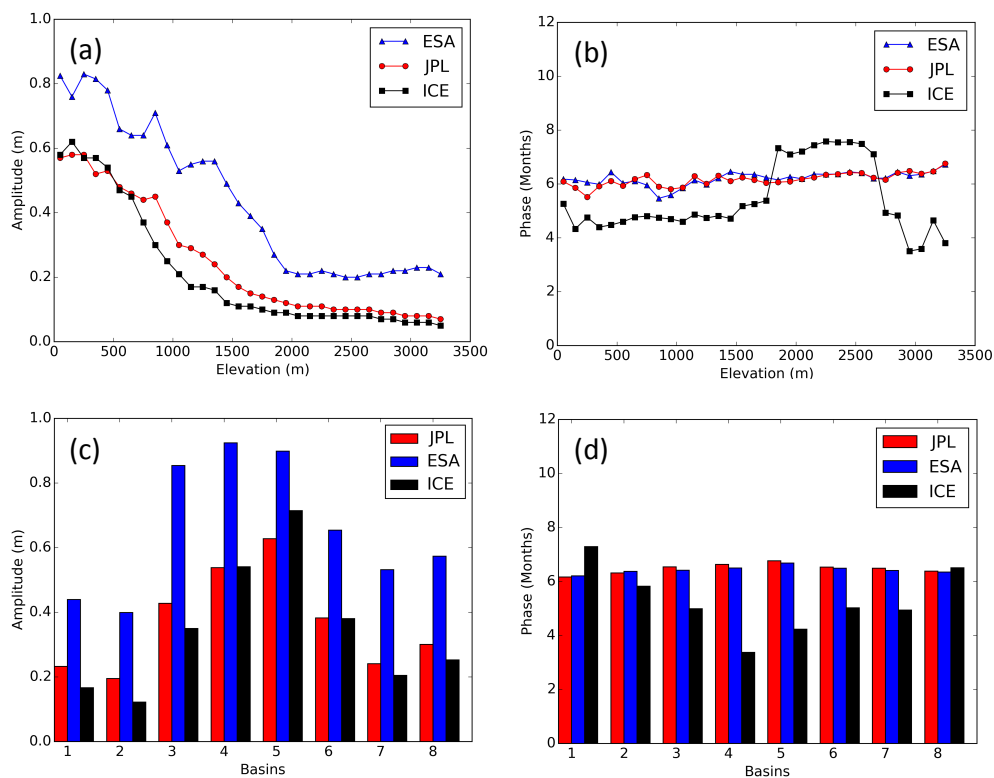
958 *visualization. The grey vertical line indicates the timing of the 2012 melt event.*



959

960 *Figure 4. Surface elevation changes of the Greenland Ice Sheet from 2011-2015, based on the*
961 *surface-fit method, overlaid on CryoSat-2 hill-shaded DEM (Jul-2010 to Feb-2015).*

962



963

964 *Figure 5: Estimated seasonal amplitude (a,c) and phase of the maximum amplitude (b,d) from*
 965 *the surface-fit method for CryoSat-2 [ESA (blue) and JPL (red)] compared to ICESat (ICE,*
 966 *black)). Values are compared using a search radius of 500 m and the phase offset is referenced*
 967 *from 1st of January*

968

969

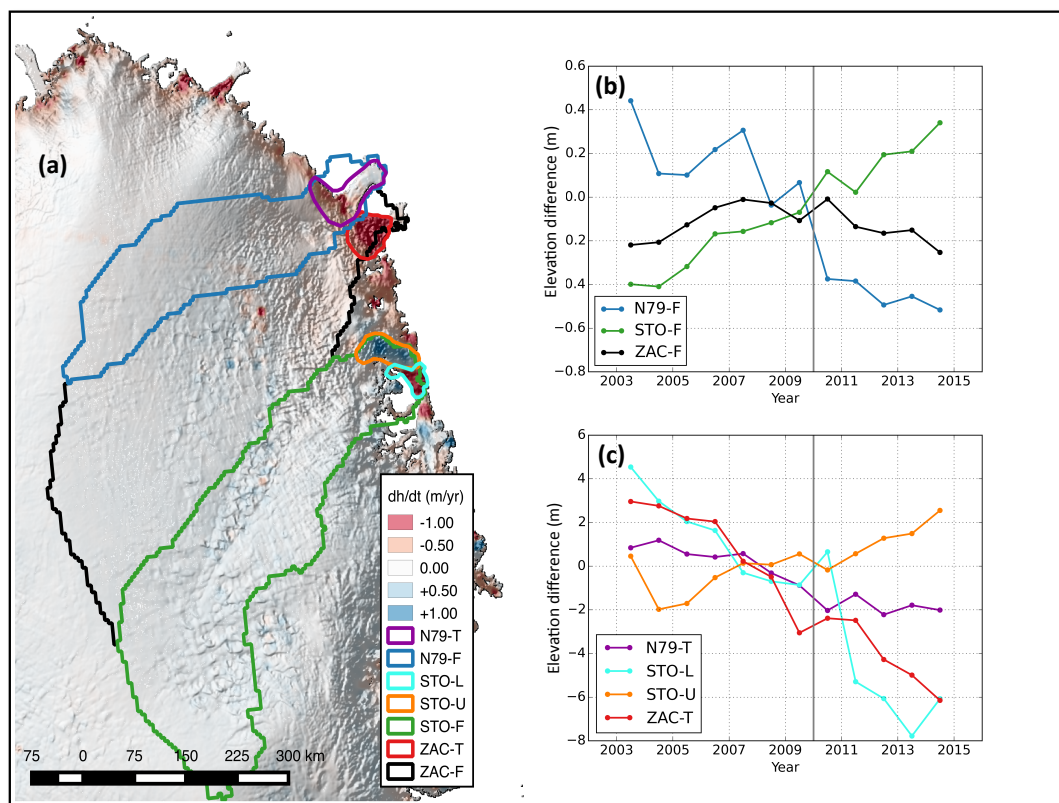
970

971

972

973

974



975

976 *Figure 6: Northeast part of the Greenland Ice Sheet showing surface elevation change (a) from*

977 *CryoSat-2 JPL-solution (2011-2015), with corresponding hydrological basin outlines. The*

978 *hydrological basins are separated into full basins size (b) and to the terminus areas (c). Sub-*

979 *figures (b) and (c) shows a merged 12 year annual elevation time series from ICESat and*

980 *CryoSat-2 for each color-coded area in (a). The derived elevation time series was formed using*

981 *the surface-fit method described in Section (3.1). The elevation change map is overlaid onto the*

982 *CryoSat-2 hill shaded DEM based on surface heights from Jul-2010 to Feb-2015.*

983

984